Dual-modality digital holographic and polarization microscope to quantify phase and birefringence signals in biospecimens with a complex microstructure

VAN K. LAM,[1] THUC PHAN,[2] KHANH LY,[1] XIAOLONG LUO,[3] GEORGE NEHMETALLAH,[2] AND CHRISTOPHER B. RAUB[1,*] (iD)

[1]*Department of Biomedical Engineering, The Catholic University of America, 620 Michigan Avenue NE, Washington, DC 20064, USA*
[2]*Department of Electrical Engineering and Computer Science, The Catholic University of America, 620 Michigan Avenue NE, Washington, DC 20064, USA*
[3]*Department of Mechanical Engineering, The Catholic University of America, 620 Michigan Avenue NE, Washington, DC 20064, USA*
[*]*raubc@cua.edu*

Abstract: Optical phase and birefringence signals occur in cells and thin, semi-transparent biomaterials. A dual-modality quantitative phase and polarization microscope was designed to study the interaction of cells with extracellular matrix networks and to relate optical pathlength and birefringence signals within structurally anisotropic biomaterial constructs. The design was based on an existing, custom-built digital holographic microscope, to which was added a polarization microscope utilizing liquid crystal variable retarders. Phase and birefringence channels were calibrated, and data was acquired sequentially from cell-seeded collagen hydrogels and electrofabricated chitosan membranes. Computed phase height and retardance from standard targets were accurate within 99.7% and 99.8%, respectively. Phase height and retardance channel background standard deviations were 35 nm and 0.6 nm, respectively. Human fibroblasts, visible in the phase channel, aligned with collagen network microstructure, with retardance and azimuth visible in the polarization channel. Electrofabricated chitosan membranes formed in 40 μm tall microfluidic channels possessed optical retardance ranging from 7 to 11 nm, and phase height from 37 to 39 μm. These results demonstrate co-registered dual-channel acquisition of phase and birefringence parameter maps from microstructurally-complex biospecimens using a novel imaging system combining digital holographic microscopy with voltage-controlled polarization microscopy.

1. Introduction

Optical signals endogenous to cells, tissues, and biomaterials allow non-invasive imaging of biological specimens without the disruption caused by various cell and molecular labeling methods. Endogenous optical signals arise from the biochemistry, nano-, and microstructure of imaged biospecimens, and include autofluorescence [1,2], infrared [3] and Raman spectral signals [4], single photon elastic scattering [5], second harmonic generation [2,6], optical phase [7,8], and birefringence signals [9,10]. Endogenous signals often have multiple dependencies on specimen properties. For example, birefringence relates to intra-molecular bond polarizability and also inter-molecular organization, through form and intrinsic components, respectively [11]. In contrast, optical phase height signals depend on specimen thickness and the index of refraction along the path of light projected through the specimen and imaged at each pixel [12,13]. Microscopy using endogenous optical signals is label-free, and thus is less likely to perturb living cells or labile ultrastructural features of imaged biospecimens.

Optical phase and birefringence are two label-free signals endogenous to many biospecimens, comparison of which in biospecimens is highly informative. Local solid-phase density scales directly with both signals due to the direct effect of material density on index of refraction mismatch with water in hydrated specimens [14]. Optical pathlength [15] and optical retardance [16] also both scale with specimen thickness. On the other hand, uniaxial birefringence is sensitive to intra- and inter-molecular orientation creating a fast and slow axis with different indices of refraction, as described in the Appendix of [17]. Optical retardance is proportional to birefringence (the refractive index difference parallel versus perpendicular to the optical axis) times the sample thickness [16–19]. Optical phase signals without polarization selectivity are insensitive to the orientation dependence of the index of refraction. The origins of these two signals suggest that they will co-occur in many specimens with double refraction but will also have independent components, making them attractive signals for dual-modality imaging. Indeed, several reports describe dual-modality instruments that image both optical phase and birefringence [20–24]. Many such current instruments either utilize tomography (rather than microscopy); or use a single illumination source, which is problematic for imaging turbid biospecimens, as explained in the rationale for this study below.

Tissue remodeling involves reciprocal interactions between cells and extracellular matrix that drive several important pathologies as well as normal tissue development and repair. For example, articular cartilage degeneration [25], atherosclerosis [26] and cancer [27] all feature extensive remodeling of the extracellular matrix (ECM) associated with upregulation of inflammatory cytokines and proteolytic enzymes. On one hand, autocrine and paracrine signals in remodeling often lead to cycles of impaired tissue homeostasis with progressive remodeling, loss of healthy tissue mechanical properties, and loss of function. On the other hand, remodeling of the wound bed by fibroblasts and other resident and recruited cells is essential to wound healing. In both normal and pathophysiological processes, local ECM density and orientation may drive interactions with cells, leading to effects such as cell spreading, stress fiber formation [28], durotaxis (migration along a gradient of tissue stiffness) [29], and contact guidance in which cells orient and move along locally aligned ECM microstructure [30–32].

Chitosan is a versatile biomaterial that possesses both optical phase and birefringence signals [33], with its molecular organization influenced by various biofabrication conditions. In microfluidic devices, chitosan membranes have been assembled into freestanding films by flow: passing a connecting aperture between two adjacent microchannels allowing the free diffusion of hydroxyl ions to neutralize chitosan chains [34,35]. The optical retardance of the film trends from high on the source side of hydroxyl ions to low on the film-growing side, while fluorescent signal from labeled chitosan is constant across this profile [36]. Alternatively, chitosan films assembled on proximal side wall cathodes [37] or across a pore between microchannels leading to distal cathodes [38] also possess birefringence, and thus some degree of orientation, possibly due to preferential alignment of chitosan chains along a voltage gradient. Researchers are currently exploring chitosan films in microfluidics for various applications, including molecular sieves, gradient generation [39], electrode-gel interfaces [37], and construction of tissues on chips [40].

Turbid biospecimens with complex microarchitecture would be challenging to image with a bimodal digital holographic microscopy (DHM) combined with traditional polarization microscopy. Laser speckle patterns manageable during phase reconstruction would tend to drastically reduce contrast in the polarization channel. Further, birefringence contributes to optical phase signal, so that optical phase maps would depend on local optical axis orientation with respect to the laser polarization of a single, linear polarized laser illumination source were used to collect both channels. Finally, manual or motorized rotation of polarization elements is laborious, slow, and introduces further measurement errors. In this study, we hypothesized that highly accurate and independent optical phase and birefringence parameter maps of turbid biospecimens could be created from a bimodal DHM and quantitative polarization microscope.

This was achieved by using two independent light sources, one coherent and one incoherent for phase and birefringence channels, respectively; and voltage-controlled liquid crystal variable retarders for fast and sensitive acquisition of polarization images.

The resulting bimodal instrument allowed direct comparison of the optical phase and birefringence parameters in cell-seeded collagen constructs and electrodeposited chitosan films. In the former case, the morphology of adherent cells detected by the optical phase height should be parallel to the direction of underlying collagen network alignment, detected by polarized light imaging. In the latter case, comparison of optical phase and birefringence signals in chitosan membranes should reveal information relevant to the fabrication conditions and molecular organization. The polarization microscope was based on one described by Oldenbourg [41,42]. The DHM was a custom-built existing off-axis, bi-telecentric design with a Mach-Zender interferometer configuration [8]. The two channels were collected sequentially but rapidly by means of a flip stage placing the illumination and polarization state generator into/out of the imaging path. Separate calibration of DHM and polarization channels was followed by co-registration using a printed phase target. Chitosan films fabricated in microfluidic channels and cell-seeded collagen tissue constructs were imaged with the dual-modality instrument and separately, with a conventional quantitative polarized light microscope using a previously described set of acquisition techniques [10] to determine optical retardance and orientation maps. Results demonstrate the accuracy of the dual holographic and polarization microscope, and the sensitivity to chitosan molecular organization in microfluidic biofabrication platforms and to cells and collagen microstructure within *in vitro* tissue constructs. Turbid specimens were found to interact with laser speckle to produce non-uniform polarization backgrounds that produced errors in polarization parameter maps. This problem was eliminated by using an incoherent illumination source for the polarization channel. Therefore, the novel bimodal imaging system is particularly well-suited for mapping optical phase and polarization parameters from turbid specimens with complex microarchitectures.

2. Materials and methods

2.1. Cell culture

An immortalized human gingival fibroblast cell line (HGF, T0026, Applied Biological Materials, Inc., BC, Canada) was cultured on tissue treated polystyrene dishes, in standard tissue culture conditions of 37°C, 5% CO_2, and 100% humidity (HERAcell 150i, Thermo Fisher Scientific, MA). Cells were fed with Prigrow III Medium (Applied Biological Materials, Inc.) containing 10% fetal bovine serum (Corning, NY) and a 1% solution of antibiotics (Penicillin-Streptomycin, Corning, NY). Cells were fed every two days and split when reaching confluency, using trypsin.

2.2. Collagen preparation

Rat tail type 1 collagen hydrogels at 4 mg/ml were prepared from 8.15 and 10.21 mg/ml stock solutions (#354249, Corning, NY). Stock collagen was mixed with 10X phosphate buffered saline (PBS) (Sigma-Aldrich, St. Louis, MO) to bring the PBS concentration to 1X., The PBS contained phenol red to assess the pH. A balance of double-distilled deionized (D.I.) water was added to the mixture. The solution was titrated with 0.1 M sodium hydroxide to a pH of 7.4–7. 6, shifting the color from yellow to light red. The pH-adjusted collagen solution was then added to glass-bottomed Petri dishes (Cellvis, Mountain View, CA) to cover the glass surface. A micropipette was set to 2 μl and used to create 4–5 air bubbles in the collagen solution. Collagen-containing Petri dishes were gently wrapped with parafilm to avoid evaporation and left to polymerize inside the incubator for 30 minutes at 37°C. Then, 25,000 fibroblasts were seeded onto the surface of the gel, allowed to adhere for 1 hour, and finally, nutrient media was added before culturing the constructs for 24–48 hours.

2.3. Chitosan membrane fabrication

A 0.5% w/v alginate solution was prepared by dissolving medium-viscosity sodium alginate powder extracted from brown algae (Sigma-Aldrich, St. Louis, MO) in D.I. water and stirred overnight. The alginate solution was adjusted to pH 6.0 for chitosan membrane electrofabrication. The 0.5% w/v chitosan solution was prepared by dissolving 85% deacetylated, medium molecular weight chitosan flakes (Sigma-Aldrich, St. Louis, MO) in D.I. water, titrated with 1M hydrochloric acid dropwise to pH 2 and left stirring overnight. Sodium hydroxide at 1M was then added dropwise to the solution to adjust the pH to 5.5. D.I. water was added to bring the chitosan solution to its final concentration of 0.5% w/v. The resulting chitosan solution was then filtered through a funnel with pore size of 170–220 µm and used for chitosan membrane electrofabrication [38].

Chitosan membranes were fabricated in microfluidic devices comprised of poly(dimethylsiloxane) (PDMS) microchannels (Fig. 1). The microchannels were bonded to a cleaned glass slide using oxygen plasma. The device consisted of two microchannels with two inputs and two outputs as shown in Fig. 1(A). Two microchannels of 500 µm x 40 µm in width and height were connected at a 60-µm-wide aperture. Two metal couplers 22 ga × 8 mm (Instech Laboratories, Inc., Plymouth Meeting, PA), functioning as both capillary connectors and distal electrodes, were inserted into one terminal of each microchannel, while the other terminals of the microchannels were left open. Once chitosan and alginate solutions were introduced into the microchannels by syringe pumps (NE-1000, New Era Pump Systems, Inc., Farmingdale, NY) at the flow rate of 1 µL/min, an air bubble was naturally trapped in the aperture between the two solutions due to the hydrophobicity of PDMS (Fig. 1(A), 1(B)). The pumps were stopped, and the air bubble was then vacuumed out of the PDMS device with an add-on vacuuming chamber based on the gas permeable property of PDMS (Fig. 1(B)) as previously reported [43]. A polyelectrolyte complex membrane (PECM) was spontaneously formed upon the contact of the positively charged chitosan and negatively charged alginate solutions (Fig. 1(C)). Next, a direct current of 60 A/m^2 from a power supply (2450 Keithley SourceMeter, Keithley Instruments, Cleveland, OH) was applied through the distal electrodes allowing chitosan membrane growth on the PECM over time as shown in Fig. 1(D) and
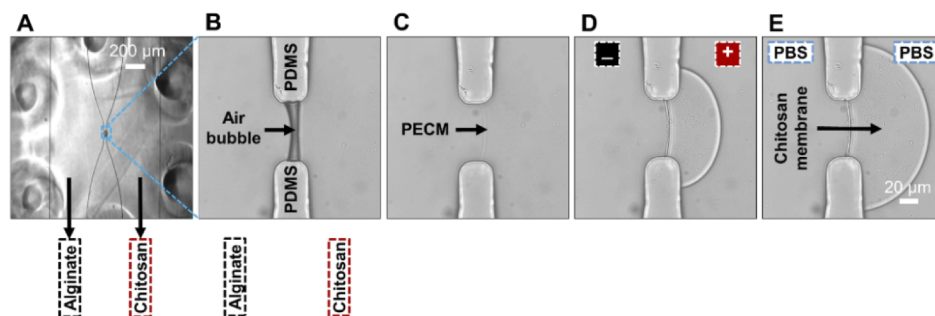

Fig. 1. Microfluidic electrofabrication of a chitosan membrane with distal electrodes. (A) A micrograph of the microchannels filled with alginate (0.5% w/v, pH = 6.0) and chitosan (0.5% w/v, pH = 5–5.5) solutions under an add-on vacuuming chamber; (B) an air bubble trapped inside the aperture between microchannels due to hydrophobicity of the PDMS device; (C) a thin polyelectrolyte complex membrane (PECM) was instantaneously formed due to interaction between carboxyl groups of alginate and amine groups of chitosan; (D) an insoluble chitosan membrane grew upon the PECM due to a flux of OH$^-$ driven by an applied electrical field through distal electrodes, triggering the deposition of chitosan; and (E) the final chitosan membrane after rinsing with phosphate buffer saline. Scale bars: 200 µm in (A) and 20 µm in (B) to (E).

1(E). All membranes in microchannels were electrofabricated within 10 min, manually rinsed with PBS, and stored at 4°C prior to imaging.

2.4. DHM channel set-up

An off-axis bi-telecentric DHM system was used to collect digital holograms and derive reconstructed phase maps (Fig. 2(A)). The microscope was custom-built, as reported in [8]. DHM lateral resolution was 1.2 µm with a 0.18×0.18 µm pixel dimensions for lateral reconstruction. A 633 nm HeNe laser was used to generate objective and reference beams. Interference patterns created by these two beams recombined at a beam splitter were imaged by a 1.3 MP CMOS camera (Lumenera Corporation, Inc., Ontario, Canada), with the reference arm angled slightly by one mirror to produce an off-axis hologram. Phase height map reconstruction was performed using principal component analysis (PCA) to cancel the main hologram aberrations, while Zernike polynomial surface fitting was applied to cancel high-order aberrations. A detailed reconstruction method to remove aberrations from holograms acquired with this instrument was described previously. In this study, the refractive index difference (Δn) used to reconstruct phase height maps for chitosan membrane and a cell-collagen sample was 0.0189 and 0.044, respectively. Phase height map images were reconstructed using Matlab as described previously [12].
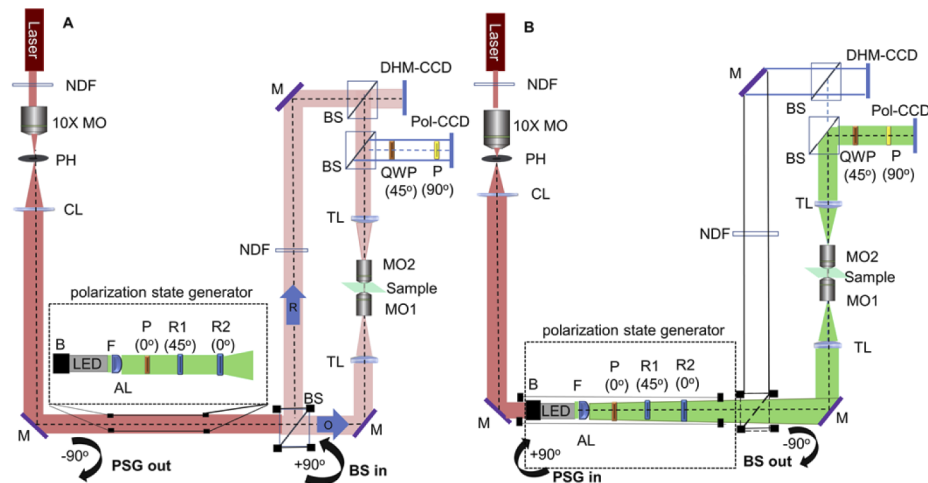

Fig. 2. A schematic of a dual DHM-Polarization modular system (A) when the DHM channel is in use, and (B) when the polarization channel is in use. Abbreviations are: Neutral Density Filter (NDF), Collimating Lens (CL), Mirror (M), Pin Hole (PH), Microscopy Objective (MO), Polarizer (P), Filter (F); Aspheric Lens (AL); Tube Lens (TL), Quarter Wave Plate (QWP), Light Block (B), Beam Splitter (BS), and Polarization State Generator (PSG).

2.5. Polarized channel set-up

A polarized light channel was constructed following guidelines published previously [42], with some modifications and innovations for dual modality imaging with the DHM. Laser illumination propagated through the polarization elements was found to produce a non-uniform polarization background, leading to errors in polarization parameter maps, so incoherent LED illumination was used instead. This second illumination source also ensured the complete independence of phase and polarization signals. The setup consisted of a mounted LED source, a 547 nm green interference filter, an aspheric lens, a polarizer and two liquid crystal variable retarders (LCVR)

comprising a polarization state generator, a condenser, microscopy objectives, a left-circular analyzer and a CCD added to the existed DHM set up (Fig. 2(B)). It should be noted that MO1 and MO2 in Fig. 2 were 10x and 20x Plan Fluor objectives (Nikon) with a high level of correction for chromatic aberration, to reduce errors between the polarization channel, centered at 547 nm, and the DHM channel at 633 nm. The illumination-side optics were installed into a cage system attached on a 90° flip mount, which allowed repeated switching between DHM and polarization illumination/detection setups. The polarization state generator was made from a linear polarizer set at 45° with respect to the slow axis of the first LCVR, itself aligned at 45° with respect to the slow axis of the second LCVR. The left-circular analyzer consisted of a quarter wave plate (QWP) and another linear polarizer parallel to the generating LCVR and polarizer principal axes. Polarized images were collected by a 1.3 MP thermo-electrically cooled CCD (Infinity 3-1, Lumenera Corporation). Polarization maps were compared to those computed from images collected on a commercial polarized light microscope (MT 9950, Meiji Techno Inc.). Image acquisition from Meiji-type polarization microscopes and subsequent computational processing of retardance and azimuth maps have been reported in detail previously [10,36,37]. Polarization filters were manually rotated with angular readouts from a Vernier scale, with resolution of 2°. For a given pixel, retardance and azimuth were derived from a local minimum intensity (extinction) recorded across a series of images acquired using the Sénarmont technique adapted for digital analysis [16] and the azimuth determining technique of [18], respectively. Images were scaled to the same size by imaging a micrometer slide and measuring μm/pixel. For clarity, background within the microfluidic channel was segmented and removed from azimuth maps obtained with both the Meiji and polarization system, while background in the retardance parameter maps was retained. Image segmentation was performed manually in ImageJ version 1.53c.

2.6.　Brief theory of polarization microscopy with variable retarders

A specimen is considered to have retardance magnitude R and slow axis azimuth ϕ distributed in the Cartesian coordinate x-y plane, termed the specimen plane. Using the instrument described above, retardance values up to π radians (273.5 nm for a 547 nm wavelength source) and azimuth values from 0° to 180° can be measured. Birefringence maps are calculated from intensity values of images collected under different voltage settings applied to liquid crystal variable retarders in the polarization state generator [42]. This approach is rapid (~seconds) and requires no moving parts during acquisition.

Elliptical polarization states are generated by a pair of LCVRs (LCC1423-A, Thorlabs) which alter linearly polarized light passing through a fixed polarizer. The slow axes of LC-A and LC-B are aligned at 45° and 0° with respect to the principal axis of the linear polarizer. A Jones vector represents light polarization after passing through the two retarders is:

$$E = \begin{pmatrix} \cos\frac{\alpha}{2}\exp\left(-i\frac{\beta}{2}\right) \\ -i\sin\frac{\alpha}{2}\exp\left(i\frac{\beta}{2}\right) \end{pmatrix} \tag{1}$$

where α and β refer to the retardance of LC-A and LC-B, respectively, at given voltage settings.

The final intensity, transmitted through the specimen, quarter waveplate, linear analyzer, and recorded at the camera, $I(\alpha, \beta, x, y)$, can then be derived as:

$$I(\alpha,\beta,x,y) = \tfrac{1}{2}\tau(x,y)I_{max}(x,y)[1 + \sin\alpha\cos\beta\cos\Gamma(x,y)-$$
$$\sin\alpha\sin\beta\cos2\theta(x,y)\times\sin\Gamma(x,y) + \cos\alpha\ \sin2\theta(x,y)\sin\Gamma(x,y)]+ \tag{2}$$
$$I_{min}(x,y)$$

where $I_{max}(x, y)$ is the illumination intensity distribution, $\tau(x, y)$ is an isotropic attenuation factor due to the specimen, and $I_{min}(x, y)$ is specimen background illumination. $\Gamma(x, y)$ and $\theta(x, y)$ are the desired retardance and azimuth maps, respectively.

2.7. Polarized light image calibration, acquisition and processing

Calibration was initially performed to determine LCVR voltage settings that provided good polarization inputs for robust retardance calculations, and to find retardance background. The calibration was performed using software provided with LCVR controllers (LCC25, Thorlabs). Retardance values of the two LCVRs are slightly tuned by either increasing or decreasing applied voltages to achieve five desired settings ($\sum_1$, $\sum_2$, $\sum_3$, $\sum_4$, $\sum_5$; Table 1). The first setting or "extinction setting", $\sum_1$, was determined by initially setting $\alpha = 90°$ and $\beta = 180°$. Then, α and β were changed incrementally and intensities were recorded and assessed until a minimum intensity was reached. A swing retardance, χ, was determined from previous experience with each specimen type (with larger χ for specimens with higher retardance) and applied in the next four polarization settings. The final four settings, if properly calibrated, should produce images with equal intensities (Fig. 3).

Table 1. Retarder settings and polarization ellipse parameters for channel calibration.

Images For Polarization Map Computation	LC-A Retardance (α) in degrees	LC-B Retardance (β) in degrees	Polarization ellipse		Optimal Intensity (I), Background
			γ major axis angle	ε auxiliary angle	
$\sum_1$	90°	180°	N/A	45°	I_1 (minimum intensity)
$\sum_2$	90° + χ	180°	0°	45°-χ/2	I_2 ($I_2 >> I_1$)
$\sum_3$	90°	180° + χ	90°	45°-χ/2	$I_3 = I_2$
$\sum_4$	90°	180° - χ	45°	45°-χ/2	$I_4 = I_2$
$\sum_5$	90° - χ	180	135°	45°-χ/2	$I_5 = I_2$

While the first setting created a right-circularly polarized beam (polarization ellipse auxiliary angle, $\varepsilon=45°$), the four other settings produced polarized beams of equal ellipticity ($\varepsilon=45°$-χ/2), distributed off longitudinal circles intersecting 4 of the 6 "poles" on the Poincaré sphere (see Supplemental Figure S1) [42]. A glass bottomed-petri dish containing 1X PBS was used as a blank sample for calibration and collecting background images. Subsequently, specimens were imaged included a zero-order quarter waveplate, a chitosan membrane fabricated in a polydimethylsiloxane channel and cell-seeded collagen gels (examples of raw polarization images in Fig. 4). The swing retardance was $\chi=90°$ for the QWP, $\chi=28.8°$ for chitosan membranes, and $\chi=14.4°$ for collagen constructs.

2.8. Image processing and analysis

Images recorded from setting 1 through setting 5 were processed for retardance and azimuth maps using algorithms published in [42]. Subsequent image analysis was performed using ImageJ (ImageJ v1.53c, public domain license, BSD-2).

Two intermediate results, *A* and *B* based on images I_1 to I_5 recorded at settings $\sum_1$ to $\sum_5$ were:

$$A = \frac{I_5 - I_2}{I_5 + I_2 - 2I_1} \cdot tan\frac{\chi}{2} \tag{3}$$

$$B = \frac{I_3 - I_4}{I_3 + I_4 - 2I_1} \cdot tan\frac{\chi}{2} \tag{4}$$

Similarly, intermediate values A_{bg} and B_{bg} from background images were also calculated. Background correction was applied by subtracting background from specimen *A* and *B* variables.
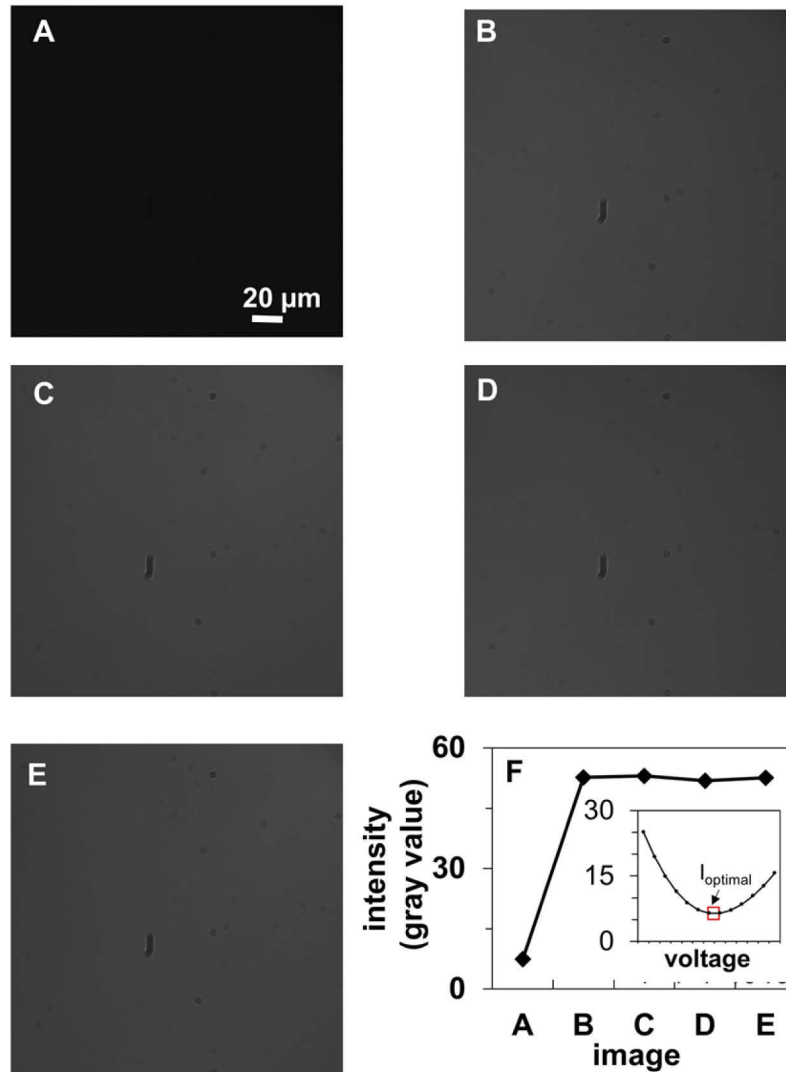
Fig. 3. Calibration procedures were performed by capturing five setting images of a background sample. (A-E) shows images of five polarization settings of a glass-bottomed petri dish containing 1X PBS. LCVR retardance values were set at settings 1 to 5. (F) depicts intensity values of the five images. An inset placed in the right corner of (F) depicts the optimal (minimal) intensity selected in setting 1. Images from A to E were used for background calculations.
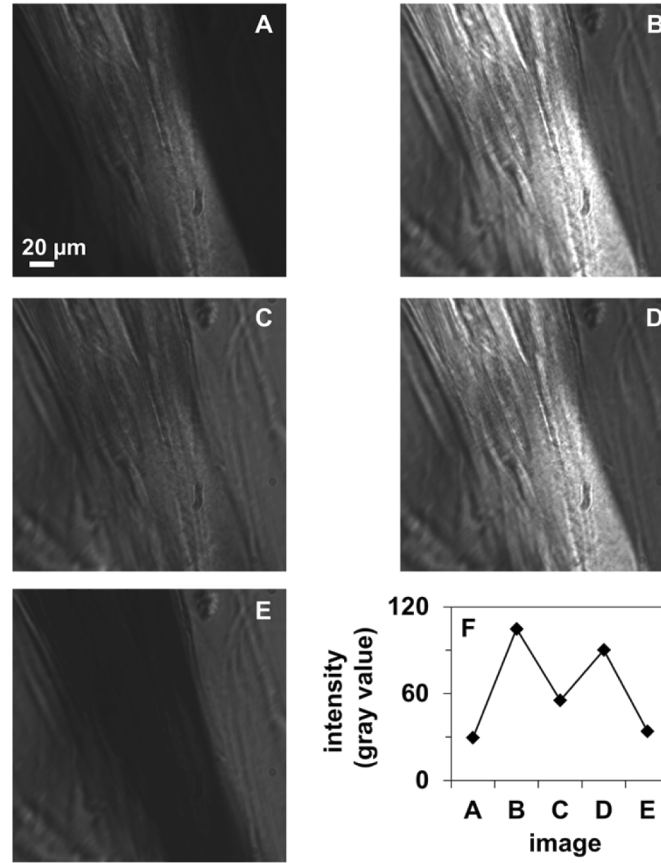
Fig. 4. Five images (A-E) of a collagen-cell construct at five polarization settings. After calibration, the five voltage settings were repeated for imaging specimens. The intensity plot (F) depicts whole image-averaged intensity in A-E.

Retardance values, Γ, and azimuth, θ, were then calculated as:

$$\Gamma = \arctan\left[\sqrt{(A - A_{bg})^2 + (B - B_{bg})^2}\right] \tag{5}$$

$$\Gamma = 180 - \arctan\left[\sqrt{(A - A_{bg})^2 + (B - B_{bg})^2}\right] \tag{6}$$

$$\theta = \frac{1}{2}arctan\left(\frac{A - A_{bg}}{B - B_{bg}}\right), \tag{7}$$

With Eq. (5) used when $I_2 + I_3 - 2\,I_1 \geq 0$ and Eq. (6) used otherwise. For imaging the QWP, a modified four-setting algorithm was used, without the first extinction setting [42].

3. Results

3.1. Dual channel accuracy and precision

Retardance (Fig. 5(A)) and azimuth maps (Fig. 5(B)) of a quarter waveplate were uniform. The measured retardance was 136.4 ± 0.6 nm (mean $\pm$ SD), close to the nominal retardance of $\frac{\lambda}{4} = 136.75$ nm. The measured azimuth was $127.7 \pm 0.9°$. The standard deviation of retardance

(background variation) on the nominally smooth waveplate was 0.6 nm (Fig. 5(A)), in comparison to 37 nm on a nominally smooth, 350 nm phase height target (see Supplemental Fig. S2). The accuracy of the calculated retardance and phase maps were 99.8% (image average from one trial: 136.4 nm vs. 136.75 nm nominal) and 99.7% (one target measurement from three trials: 350.9 nm vs. 350 nm nominal), respectively. It should be noted that three successive calibrations over two weeks using the same quarter waveplate produced image-averaged measured retardance of 126.0 ± 0.4 nm, 135.0 ± 0.5 nm, and 136.4 ± 0.6 nm, a trend reflecting the experimenter's proficiency with LCVR voltage control to best meet the criteria of Table 1, such as finding a truly minimum extinction image and subsequent background images of equal intensity. This progression in learning suggests the suitability of developing an auto-calibration procedure, in future work. The phase calibration slide was imaged three times with measured phase height of a target (the largest square in Fig. S2) 348.0 ± 37 nm, 351.5 ± 46 nm, and 353.2 ± 23 nm.
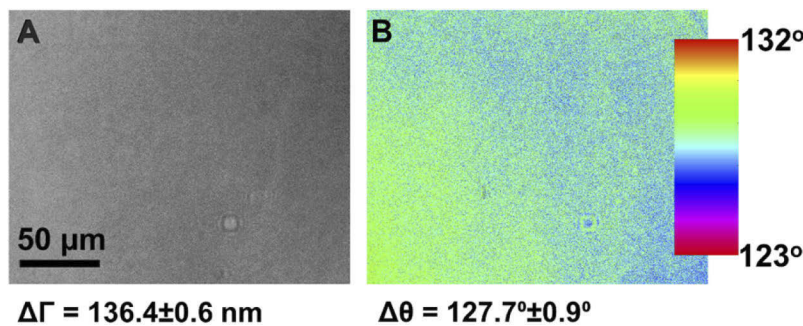

Fig. 5. Retardance map (A) and azimuth map (B) of a QWP derived from the polarization module.

3.2. Retardance and phase maps from electrofabricated chitosan membranes

An electrofabricated chitosan membrane was used to test the polarization module sensitivity. After calibration, retardance and azimuth maps were generated and compared to maps of the same membrane derived from a polarized light microscope using the **"**Sérnamont" technique updated to use digital image data [16] and an azimuth-detecting technique [10,18]. Whole-membrane averaged retardance values were 9.2 ± 2.0 nm (Fig. 6(A)) and 10.4 ± 3.0 nm (Fig. 6(B)) for the imaging module and microscope, respectively. The slow axis of the chitosan membranes ranged continuously through 140°, consistent using both imaging systems (Fig. 6(C), 6(D)). Small differences between retardance and azimuth maps computed using data from the two systems may arise from small errors in calibration of either system. The two bright spots in Fig. 6(A) may be related to errors in LCVR voltage settings for the polarization module. Differences in azimuth may relate to errors in optical axis alignment of polarization elements in either system. Further fine tuning of the polarization module calibration may require imaging of a precise birefringence standard such as an optical fiber, and/or simulation of error propagation from raw images to computed parameter maps. This fine tuning and further investigation of the chitosan membrane ultrastructure and birefringence properties are left to future studies.

   Next, retardance (Fig. 7(A), profile in 7B) and phase height maps (Fig. 7(C), profile in 7D) from polarization and DHM channels were co-registered and compared using the same chitosan membrane. Profiles through the central portion of the membrane reveal retardance dropped from 11 to 7 nm from cathode to anode side of the membrane (Fig. 7(B)), but optical phase height remained constant at around 38 μm (close to the nominal channel height of 40 μm) (Fig. 7(D)). The gradient in retardance as well as two flares in retardance near the aperture edges are apparent in an overlay of retardance and phase height maps (Fig. 7(E)). These results demonstrate that the
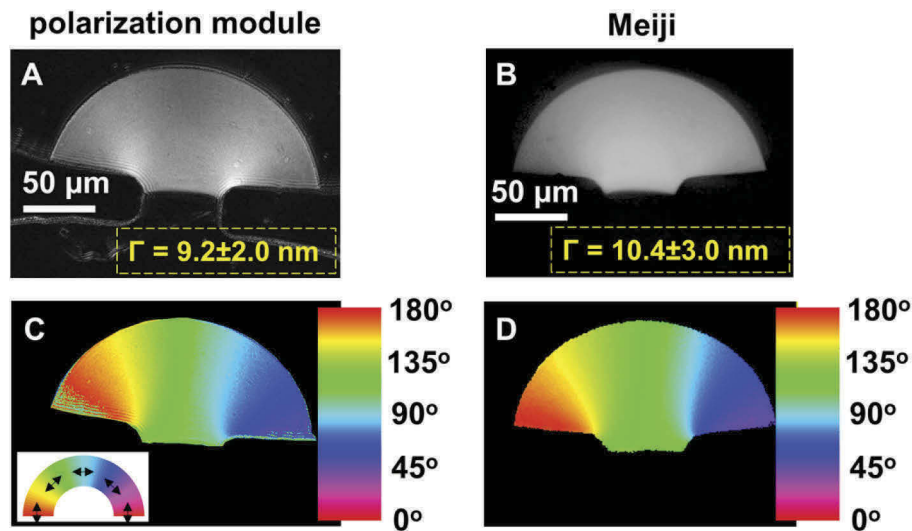
Fig. 6. Retardance (Γ, nm) map and azimuth map of a chitosan membrane collected by the polarization module (A,C) and Meiji polarization microscopes (B,D). Average ± standard deviation retardance values are printed in the Polarization module retardance map (A) and Meiji microscope retardance map (B). The "Sernamont" technique was used to compute maps the retardance in (B), with an associated technique to calculate azimuth in (D). Retardance maps were brightened to reveal spatial features. Scale bar of 50 μm is indicated.

exact same location of an electrofabricated chitosan membrane can be sequentially imaged with the newly developed dual DHM-polarization microscope. The obtained data about specimen phase and retardance together demonstrate that, although the phase height across the entire membrane was uniform, the molecular alignment within the membrane was uneven, presumably a result of the nonuniform potential gradient generated around the aperture area.

3.3. Retardance and phase maps from fibroblast-seeded collagen gels

Collagen network microstructure was aligned tangentially to the edge of bubbles placed in collagen gels during self-assembly, apparent in retardance maps (Fig. 8(A)). The co-registered optical phase height map revealed fibroblasts with long axes aligned with collagen network microstructure (Fig. 8(C)). Retardance (Fig. 8(B)) and phase height profiles (Fig. 8(D)) along co-registered maps revealed the fine structure of these two signals varied independently. Signal differences were apparent in the overlay (Fig. 8(E)). Similar trends and features were apparent in every construct examined, represented by four fields of view (Fig. 9). Retardance values from aligned collagen networks were similar from the polarization module of the DHM-polarization dual modality microscope and a standalone polarized light microscope (Fig. 10). Due to co-registration of DHM and polarization channels cell morphology, revealed in phase maps, and collagen network microstructural organization, revealed in retardance and azimuth maps, are immediately relatable. Thus, the dual DHM-polarization microscope is well-suited to determine cell-extracellular matrix mechanical interactions in the context of motility, substrate adhesion, and tissue remodeling.
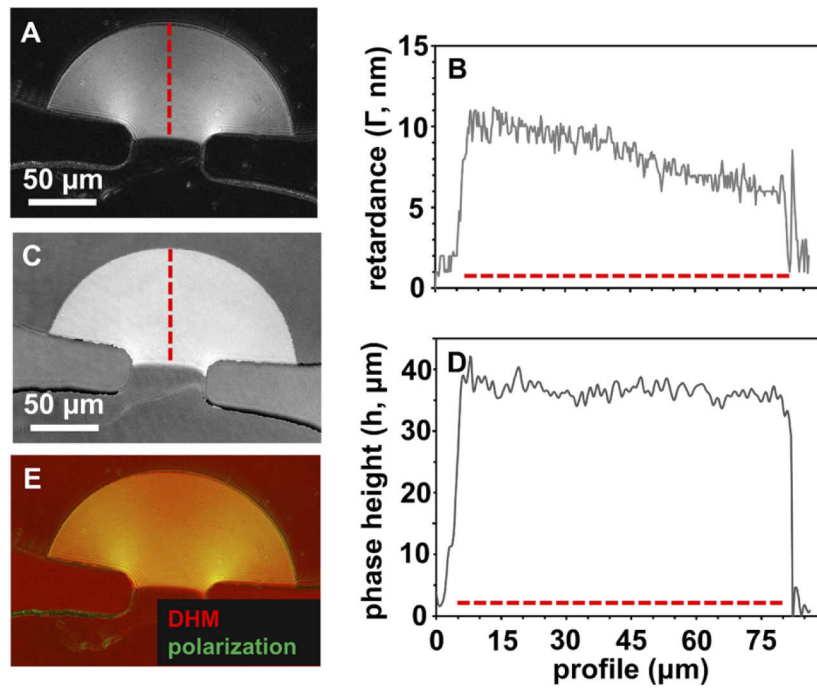
Fig. 7. Phase and retardance images of a chitosan membrane were collected simultaneously by the dual DHM-Polarization microscope. Images of a chitosan membrane imaged by Polarization (A) and DHM (C) channels. (E) is a co-registered image map of A and C in which red and green channels represent phase height and retardance signals from DHM and Polarization modules, respectively. Plots in (B) and (D) are retardance and phase height profiles indicated by the red dashed lines in (A) and (C). Scale bar is 50 μm.
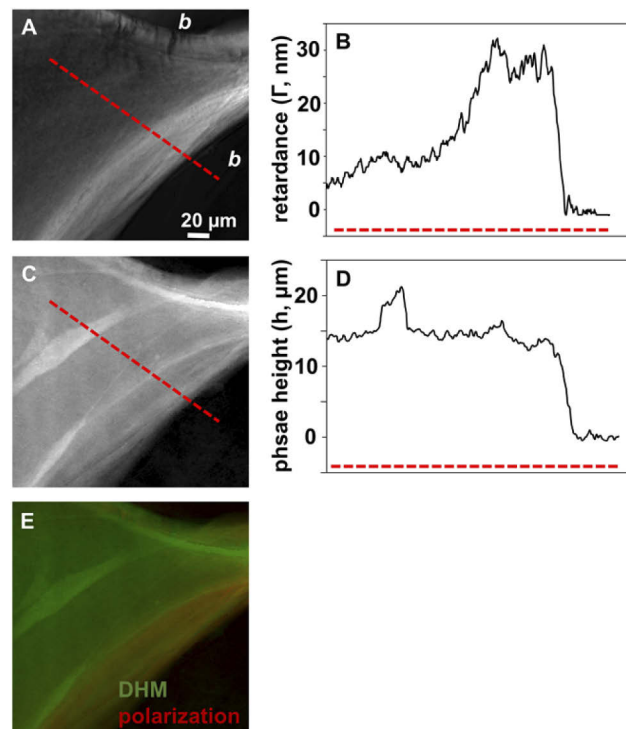
Fig. 8. Phase and retardance images of a collagen-cell sample were collected sequentially by the dual DHM-Polarization module set up. Images of the collagen region lying between two bubbles containing several HGF cells were imaged by Polarization (A) and DHM (C) channels. (E) merges A and B in which green and red channel represents phase height and retardance signals, respectively. Plots in (B) and (D) show retardance and phase height distribution profiled indicated by red dashed lines in (A) and (C). Scale bar is 50 μm. Locations where bubbles were present during self-assembly are indicated by the letter *b*.
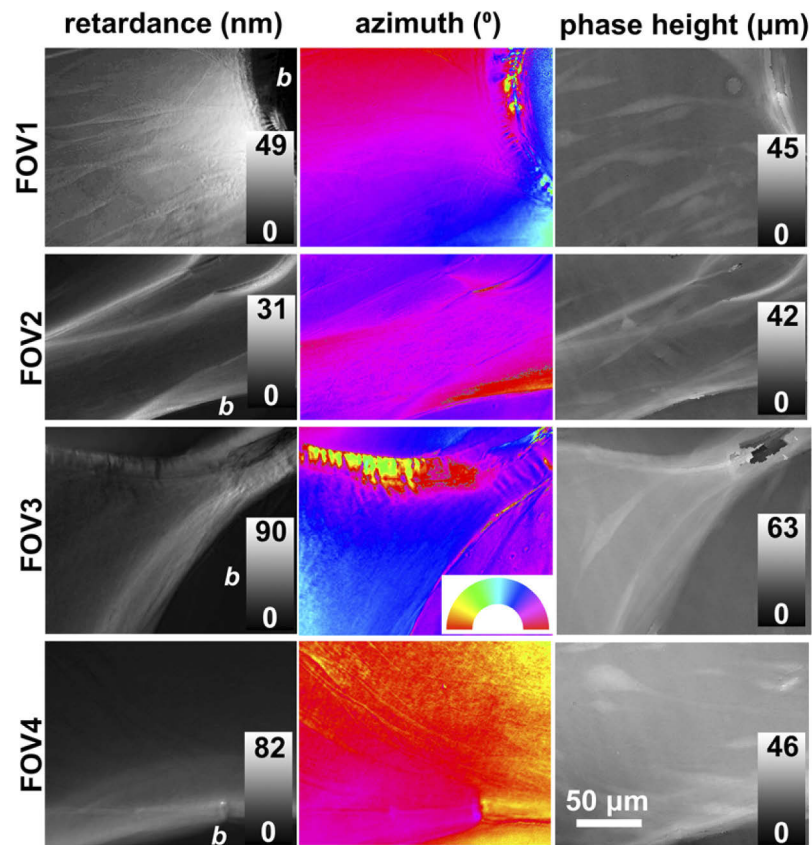
Fig. 9. Co-registered retardance, azimuth, and phase height maps from four additional fields of view (FOV1 to 4) fibroblast-seeded collagen gels. Collagen network alignment occurs near interfaces with air bubbles placed in the gel during self-assembly. Colorbars and scale are indicated. Locations where bubbles were present during self-assembly are indicated by the letter *b*.
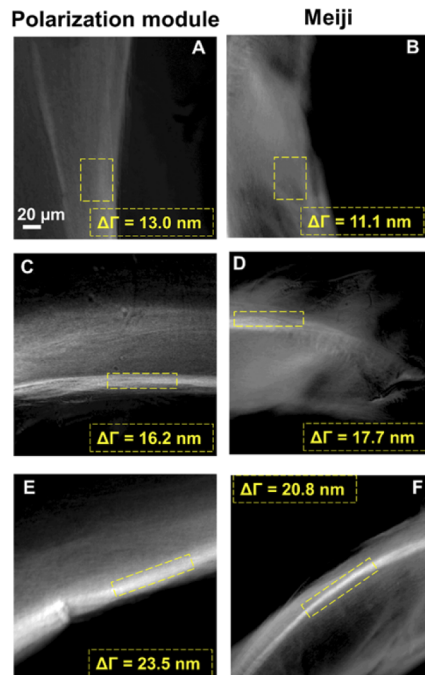
Fig. 10. Retardance maps of collagen networks surrounding the air bubbles collected from the polarization module and Meiji polarization microscopes. Similar but not co-registered structures from the same specimen were imaged in (A,B), (C,D), and (E,F), using the polarization module (A, C and E) and a Meiji polarized light microscope (B, D and F). Average retardance values within the yellow dashed boxes from each image are indicated. Scale bar is indicated.

4. Discussion

In this study, a dual-modality quantitative phase and polarization microscope was developed to map optical phase and birefringence signals in biological specimens, relating the signals and underlying microscale features to each other. Specifically, maps of optical phase height, retardance and local slow axis azimuth were generated. Polarization maps were successfully derived from several specimens with low and high birefringence signals. Retardance and azimuth maps were consistent across several specimens (chitosan and cell-seeded collagen) and two imaging systems (the polarization module and a commercial polarized light microscope). Polarization parameter maps are computed with no manual manipulation of optical components, making the technique easy to perform by an untrained end-user. The HeNe laser and LED illumination sources produce low power at the imaging plane, a requirement for nondestructive analysis of living biospecimens. Due to the two light sources and sequential acquisition, DHM and polarization channels are completely independent of each other, with no channel cross-talk. Thus, the demonstrated dual-modality imaging system enables label-free biospecimen imaging with intrinsic contrast for local optical anisotropy and optical pathlength.

Detection of chitosan optical properties is useful for applications of chitosan membranes as molecular sieves, microfluidic gradient generators, and synthetic biology interfaces. The molecular sieve activity of chitosan membranes was demonstrated by the passage of calcium ions but not macromolecules through chitosan membranes to fabricate collagen-alginate gels with spatial programmability [40]. The data of Fig. 7, revealing a constant phase height matched with a high to low retardance from cathode to anode side of the membrane, constitute a novel finding in

electrofabricated chitosan membranes. These data may indicate constant density but altered intra-and/or inter-molecular alignment from cathode to anode side of the membrane. Microfluidic flow-assembled chitosan membranes display a similar drop in retardance in the direction of membrane growth [36]. Both parameters are effective and independent optical readouts for chitosan density and alignment, respectively. Aspects of chitosan membrane molecular organization and ultrastructure influence their properties, such as mechanical modulus and porosity, and their applications, such as gradient generators [43] and as biological interfaces [44,45]. The obtained phase and birefringence information may shed light on the chitosan membrane fabrication process. For example, these optical signals are related to the electrofabrication process by which distal electrodes electrically program chitosan molecular organization within the membrane [37]. Furthermore, the molecular organizations of electrically-deposited [37] and flow-assembled [36] chitosan membranes are currently being investigated. Phase height is influenced by molecular packing density [14], while form and intrinsic birefringence are also sensitive to intra- and inter-molecular alignment of chitosan chains [11]. Combined phase and birefringence imaging of chitosan membranes during microfluidic fabrication and subsequent modification may provide data to understand subtle ultrastructural shifts within such membranes, as occurs for example upon crosslinking [46]. For these reasons, birefringence parameters from electrically and flow-assembled chitosan membranes are a topic of ongoing investigation.

Human gingival fibroblasts growing on collagen hydrogels exhibit contact guidance to align parallel with collagen network anisotropy, clearly visible in co-registered phase height and retardance maps, respectively (Figs. 9,10). It is important to note that optical retardance depends on specimen thickness and uniaxial index of refraction difference [16], the latter of which scales with both microstructural alignment and density [18]. On the other hand, optical phase height depends on specimen thickness and index of refraction values projected through the specimen [15]. The local index of refraction depends on local material composition and density/hydration [14]. Therefore, a direct comparison of local gradients in phase and birefringence signals suggest a gradient in density when both match, and a gradient in alignment when the phase height gradient is absent or opposite in direction to the retardance gradient. In collagen gels, local retardance but not phase height was often high close to interfaces with bubbles placed during self-assembly and subsequently filled with media (Figs. 9,10). This suggests collagen network alignment occurred tangential to the bubble air-liquid interface during self-assembly, without a build-up in local collagen network density. Fibroblasts respond to local collagen network microstructure by alignment parallel to the microstructural long axis, consistent with contact guidance. These results suggest that the dual-modality DHM-polarization system is well-suited to study of tissue microstructural remodeling in models of wound healing, fibrosis, *in vitro* tissue development, and the cancer microenvironment. The difficulty of finding and aligning the same field-of-view with two separate microscopes, within the larger tissue construct, demonstrates the advantage of the dual modality microscope.

The current design of the dual-modality digital holographic and polarization microscope has strengths and limitations, which future modifications will retain and address, respectively. The instrument was designed to collect transmissive signals through thin, transparent tissue constructs, such as tissues and biomaterials in microfluidic chips, or cell-seeded transparent hydrogels. Other systems that record optical phase and birefringence are single-shot or directly relate the index of refraction mismatch to birefringence measurements, so that the optical phase difference may depend on local optical axis orientation and local birefringence signal [20,23]. In contrast, the two illumination sources of the present setup 1) eliminate speckle noise from the polarization channel, while 2) allowing for the possibility of building polarization sensitivity into the DHM channel and 3) multi-wavelength imaging capability into both channels. Addition of acousto-optic tunable filters and automated shutters would eliminate the need to move the two flip stages between channel acquisitions. Alternatively, bandpass filters in front of the CCD

sensors would allow simultaneous acquisition with minimal channel cross-talk. Optical depth sectioning in the phase and polarization channels would be possible through holographic and polarization-sensitive optical coherence tomography [47–51].

5. Conclusion

In conclusion, the DHM-polarization imaging system non-invasively acquires label-free optical signals endogenous to cells, tissues and biomaterials. Phase and birefringence channels produce fine structure contrast independently, aided by sequential acquisition and independent light sources. Molecular organization and specimen height ultimately govern optical phase and retardance signals, so comparison of co-localized signal features helps to elucidate spatial trends in these properties. This is particularly fruitful when interpreting cell-extracellular matrix interactions in cell-seeded hydrogel constructs. Compared to previously published descriptions of phase and birefringence imaging systems, the currently described system is well-suited to image turbid specimens such as engineered tissue constructs and biofabricated membranes in microfluidics, contributing to further understanding of such complex biospecimens. Future applications of the imaging system will include assessment of cancer invasion in a complex *in vitro* tumor microenvironmental model. This could help identify dynamic cell migration interactions with ECM contributing to pathological progression of cancer, and potentially novel therapeutic interventions.

Disclosures. The authors declare no conflicts of interest.

Data availability. Data underlying the results presented in this paper are not publicly available at this time but may be obtained from the authors upon reasonable request.

Supplemental document. See Supplement 1 for supporting content.

References

1. S. Tomo, G. I. Miyahara, and L. E. Simonato, "History and future perspectives for the use of fluorescence visualization to detect oral squamous cell carcinoma and oral potentially malignant disorders," Photodiagnosis Photodyn Ther **28**, 308–317 (2019).
2. A. Zoumi, A. Yeh, and B. J. Tromberg, "Imaging cells and extracellular matrix in vivo by using second-harmonic generation and two-photon excited fluorescence," Proc Natl Acad Sci U S A **99**(17), 11014–11019 (2002).
3. P. G. Andrus and R. D. Strickland, "Cancer grading by Fourier transform infrared spectroscopy," Biospectroscopy **4**(1), 37–46 (1998).
4. Z. Movasaghi, S. Rehman, and I. U. Rehman, "Raman Spectroscopy of Biological Tissues," Appl. Spectrosc. Rev. **42**(5), 493–541 (2007).
5. N. N. Boustany, S. A. Boppart, and V. Backman, "Microscopic imaging and spectroscopy with scattered light," Annu. Rev. Biomed. Eng. **12**(1), 285–314 (2010).
6. C. B. Raub, V. Suresh, T. Krasieva, J. Lyubovitsky, J. D. Mih, A. J. Putnam, B. J. Tromberg, and S. C. George, "Noninvasive assessment of collagen gel microstructure and mechanics using multiphoton microscopy," Biophys J **92**(6), 2212–2222 (2007).
7. V. K. Lam, T. Nguyen, T. Phan, B. M. Chung, G. Nehmetallah, and C. B. Raub, "Machine Learning with Optical Phase Signatures for Phenotypic Profiling of Cell Lines," Cytometry **95**(7), 757–768 (2019).
8. V. K. Lam, T. C. Nguyen, B. M. Chung, G. Nehmetallah, and C. B. Raub, "Quantitative assessment of cancer cell morphology and motility using telecentric digital holographic microscopy and machine learning," Cytometry **93**(3), 334–345 (2018).
9. R. N. Huynh, B. Pesante, G. Nehmetallah, and C. B. Raub, "Polarized reflectance from articular cartilage depends upon superficial zone collagen network microstructure," Biomed. Opt. Express **10**(11), 5518–5534 (2019).
10. C. B. Raub, S. C. Hsu, E. F. Chan, R. Shirazi, A. C. Chen, E. Chnari, E. J. Semler, and R. L. Sah, "Microstructural remodeling of articular cartilage following defect repair by osteochondral autograft transfer," Osteoarthritis Cartilage **21**(6), 860–868 (2013).
11. M. Doi and S. Edwards, *The Theory of Polymer Dynamics* (Oxford University, 1986).
12. T. Nguyen, G. Nehmetallah, C. Raub, S. Mathews, and R. Aylo, "Accurate quantitative phase digital holographic microscopy with single- and multiple-wavelength telecentric and nontelecentric configurations," Appl. Opt. **55**(21), 5666–5683 (2016).

13. F. Dubois, C. Yourassowsky, O. Monnom, J. C. Legros, O. Debeir, P. Van Ham, R. Kiss, and C. Decaestecker, "Digital holographic microscopy for the three-dimensional dynamic analysis of in vitro cancer cell migration," J. Biomed. Opt. **11**(5), 054032 (2006).

14. Q. Zhang, L. Zhong, P. Tang, Y. Yuan, S. Liu, J. Tian, and X. Lu, "Quantitative refractive index distribution of single cell by combining phase-shifting interferometry and AFM imaging," Sci Rep **7**(1), 2532 (2017).

15. B. Rappaz, P. Marquet, E. Cuche, Y. Emery, C. Depeursinge, and P. Magistretti, "Measurement of the integral refractive index and dynamic cell morphometry of living cells with digital holographic microscopy," Opt. Express **13**(23), 9361–9373 (2005).

16. K. Kocsis, M. Hyttinen, H. J. Helminen, M. B. Aydelotte, and L. Modis, "Combination of digital image analysis and polarization microscopy: theoretical considerations and experimental data," Microsc. Res. Tech. **43**(6), 511–517 (1998).

17. P. L. Chandran and V. H. Barocas, "Microstructural mechanics of collagen gels in confined compression: poroelasticity, viscoelasticity, and collapse," J Biomech Eng **126**(2), 152–166 (2004).

18. J. Rieppo, J. Hallikainen, J. S. Jurvelin, I. Kiviranta, H. J. Helminen, and M. M. Hyttinen, "Practical considerations in the use of polarized light microscopy in the analysis of the collagen network in articular cartilage," Microsc. Res. Tech. **71**(4), 279–287 (2008).

19. E. Collett, *Polarized Light: Fundamentals and Applications* (Dekker, 1992).

20. N. M. Dragomir, X. M. Goh, C. L. Curl, L. M. Delbridge, and A. Roberts, "Quantitative polarized phase microscopy for birefringence imaging," Opt. Express **15**(26), 17690–17698 (2007).

21. J. Dwelle, S. Liu, B. Wang, A. McElroy, D. Ho, M. K. Markey, T. Milner, and H. G. Rylander, "3rd, "Thickness, phase retardation, birefringence, and reflectance of the retinal nerve fiber layer in normal and glaucomatous non-human primates," Invest. Ophthalmol. Vis. Sci. **53**(8), 4380–4395 (2012).

22. S. Fukuda, A. Fujita, D. Kasaragod, S. Beheregaray, Y. Ueno, Y. Yasuno, and T. Oshika, "Comparison of intensity, phase retardation, and local birefringence images for filtering blebs using polarization-sensitive optical coherence tomography," Sci Rep **8**(1), 7519 (2018).

23. C. Li, S. Chen, M. Klemba, and Y. Zhu, "Integrated quantitative phase and birefringence microscopy for imaging malaria-infected red blood cells," J. Biomed. Opt **21**(9), 090501 (2016).

24. T. Colomb, F. Durr, E. Cuche, P. Marquet, H. G. Limberger, R. P. Salathe, and C. Depeursinge, "Polarization microscopy by use of digital holography: application to optical-fiber birefringence measurements," Appl. Opt. **44**(21), 4461–4469 (2005).

25. M. M. Temple-Wong, W. C. Bae, M. Q. Chen, W. D. Bugbee, D. Amiel, R. D. Coutts, M. Lotz, and R. L. Sah, "Biomechanical, structural, and biochemical indices of degenerative and osteoarthritic deterioration of adult human articular cartilage of the femoral condyle," Osteoarthritis Cartilage **17**(11), 1469–1476 (2009).

26. M. R. Ward, G. Pasterkamp, A. C. Yeung, and C. Borst, "Arterial remodeling. Mechanisms and clinical implications," Circulation **102**(10), 1186–1191 (2000).

27. R. Malik, P. I. Lelkes, and E. Cukierman, "Biomechanical and biochemical remodeling of stromal extracellular matrix in cancer," Trends Biotechnol **33**(4), 230–236 (2015).

28. A. J. Engler, S. Sen, H. L. Sweeney, and D. E. Discher, "Matrix elasticity directs stem cell lineage specification," Cell **126**(4), 677–689 (2006).

29. C. M. Lo, H. B. Wang, M. Dembo, and Y. L. Wang, "Cell movement is guided by the rigidity of the substrate," Biophys J **79**(1), 144–152 (2000).

30. V. H. Barocas and R. T. Tranquillo, "A finite element solution for the anisotropic biphasic theory of tissue-equivalent mechanics: the effect of contact guidance on isometric cell traction measurement," J Biomech Eng **119**(3), 261–268 (1997).

31. V. H. Barocas and R. T. Tranquillo, "An anisotropic biphasic theory of tissue-equivalent mechanics: the interplay among cell traction, fibrillar network deformation, fibril alignment, and cell contact guidance," J Biomech Eng **119**(2), 137–145 (1997).

32. P. P. Provenzano, K. W. Eliceiri, J. M. Campbell, D. R. Inman, J. G. White, and P. J. Keely, "Collagen reorganization at the tumor-stromal interface facilitates local invasion," BMC Med **4**(1), 38 (2006).

33. K. L. Ly, P. Hu, L. H. P. Pham, and X. Luo, "Flow-assembled chitosan membranes in microfluidics: recent advances and applications," J. Mater. Chem. B **9**(15), 3258–3283 (2021).

34. G. W. Rubloff, W. E. Bentley, X. L. Luo, H. C. Wu, and J. Betz, "Air bubble-initiated biofabrication of freestanding, semi-permeable biopolymer membranes in PDMS microfluidics," Biochem. Eng. J. **89**, 2–9 (2014).

35. P. Pham, T. Vo, and X. Luo, "Steering air bubbles with an add-on vacuum layer for biopolymer membrane biofabrication in PDMS microfluidics," Lab Chip **17**(2), 248–255 (2017).

36. K. Li, S. O. Correa, P. Pham, C. B. Raub, and X. Luo, "Birefringence of flow-assembled chitosan membranes in microfluidics," Biofabrication **9**(3), 034101 (2017).

37. K. Yan, Y. Liu, J. Zhang, S. O. Correa, W. Shang, C. C. Tsai, W. E. Bentley, J. Shen, G. Scarcelli, C. B. Raub, X. W. Shi, and G. F. Payne, "Electrical Programming of Soft Matter: Using Temporally Varying Electrical Inputs To Spatially Control Self Assembly," Biomacromolecules **19**(2), 364–373 (2018).

38. P. Hu, S. A. Rooholghodos, L. H. Pham, K. L. Ly, and X. Luo, "Interfacial Electrofabrication of Freestanding Biopolymer Membranes with Distal Electrodes," Langmuir **36**(37), 11034–11043 (2020).

39. X. Luo, T. Vo, F. Jambi, P. Pham, and J. S. Choy, "Microfluidic partition with in situ biofabricated semipermeable biopolymer membranes for static gradient generation," Lab Chip **16**(19), 3815–3823 (2016).
40. S. O. Correa, X. Luo, and C. B. Raub, "Microfluidic fabrication of stable collagen microgels with aligned microstructure using flow-driven co-deposition and ionic gelation," J. Micromech. Microeng. **30**(8), 085002 (2020).
41. S. B. Mehta, M. Shribak, and R. Oldenbourg, "Polarized light imaging of birefringence and diattenuation at high resolution and high sensitivity," J. Opt. **15**(9), 094007 (2013).
42. M. Shribak and R. Oldenbourg, "Techniques for fast and sensitive measurements of two-dimensional birefringence distributions," Appl. Opt. **42**(16), 3009–3017 (2003).
43. K. L. Ly, C. B. Raub, and X. Luo, "Tuning the porosity of biofabricated chitosan membranes in microfluidics with co-assembled nanoparticles as templates," Mater. Adv. **1**(1), 34–44 (2020).
44. T. Vo, S. B. Shah, J. S. Choy, and X. Luo, "Chemotropism among populations of yeast cells with spatiotemporal resolution in a biofabricated microfluidic platform," Biomicrofluidics **14**(1), 014108 (2020).
45. P. L. H. Pham, S. A. Rooholghodos, J. S. Choy, and X. L. Luo, "Constructing Synthetic Ecosystems with Biopolymer Fluitrodes," Adv. Biosys. **2**(3), 1700180 (2018).
46. P. Hu, C. B. Raub, J. S. Choy, and X. Luo, "Modulating the properties of flow-assembled chitosan membranes in microfluidics with glutaraldehyde crosslinking," J. Mater. Chem. B **8**(12), 2519–2529 (2020).
47. J. E. Park, Z. Xin, D. Y. Kwon, S. W. Kim, H. Lee, M. J. Jung, S. Tang, T. Y. Ko, J. H. Choi, J. H. Kim, Y. C. Ahn, and C. Oak, "Application of Polarization Sensitive-Optical Coherence Tomography to the Assessment of Phase Retardation in Subpleural Cancer in Rabbits," Tissue Eng Regen Med **18**(1), 61–69 (2021).
48. S. Fukuda, G. Kishino, S. Hoshi, S. Beheregaray, Y. Ueno, M. Fukuda, D. Kasaragod, Y. Yasuno, and T. Oshika, "Repeatability of corneal phase retardation measurements by polarization-sensitive optical coherence tomography," Invest. Ophthalmol. Vis. Sci. **56**(5), 3196–3201 (2015).
49. M. Pircher, E. Goetzinger, R. Leitgeb, and C. K. Hitzenberger, "Transversal phase resolved polarization sensitive optical coherence tomography," Phys. Med. Biol. **49**(7), 1257–1263 (2004).
50. E. Gotzinger, M. Pircher, M. Sticker, A. F. Fercher, and C. K. Hitzenberger, "Measurement and imaging of birefringent properties of the human cornea with phase-resolved, polarization-sensitive optical coherence tomography," J. Biomed. Opt. **9**(1), 94–102 (2004).
51. C. Hitzenberger, E. Goetzinger, M. Sticker, M. Pircher, and A. Fercher, "Measurement and imaging of birefringence and optic axis orientation by phase resolved polarization sensitive optical coherence tomography," Opt. Express **9**(13), 780–790 (2001).